







In situ synthesis, structural chemistry and vibrational spectroscopy of Zn-doped $\text{Ca}_5\text{Mg}_4(\text{VO}_4)_6$

Anna S. Tolkacheva ^{a*} , Sergey N. Shkerin ^a , Sofya A. Petrova ^b ,
Olga M. Fedorova ^b , Svetlana G. Titova ^b , Ivan I. Leonidov ^{a*} 

a: Institute of High-Temperature Electrochemistry, 620990 Ekaterinburg, Russia

b: Institute of Metallurgy, 620016 Ekaterinburg, Russia

* Corresponding authors: asergeevnatolkacheva@gmail.com; ivanleonidov@ihim.uran.ru

This paper belongs to the Regular Issue.

© 2021, The Authors. This article is published in open access form under the terms and conditions of the Creative Commons Attribution (CC BY) license (<http://creativecommons.org/licenses/by/4.0/>).



Abstract

The phase formation of the solid solution $\text{Ca}_5\text{Mg}_{4-x}\text{Zn}_x(\text{VO}_4)_6$ ($0 \leq x \leq 4$) was studied *in situ* using differential scanning calorimetry and high-temperature X-Ray powder diffraction (XRPD). XRPD analysis shows the appearance of unavoidable secondary pyrovanadate phases using conventional synthesis methods. The local structure of the solid solution was verified by vibrational spectroscopy. The analysis of the infrared and Raman spectroscopy data allows establishing the main features between vanadate garnets and their isostructural analogs among natural silicates.

Keywords

crystal structure
vibrational spectroscopy
X-ray diffraction
ceramics
differential scanning calorimetry
pyrovanadate
garnet

Received: 18.08.2021

Revised: 17.03.2022

Accepted: 17.03.2022

Available online: 23.03.2022

1. Introduction

A wide range of compounds with the general formula $\text{A}_3\text{B}_2\text{V}_3\text{O}_{12}$ that belong to calcium vanadate garnets is known nowadays. This system includes complex oxides with substitution of calcium ions in A position by alkaline, (Li, Na, K), alkaline-earth (Sr) and other metal cations like Cu, Ag, Cd, Pb [1, 2]. Heterovalent substitution in B position in the garnet structure $\text{A}_3\text{B}_2\text{V}_3\text{O}_{12}$ ($\text{B} = \text{Mg}^{2+}, \text{Mn}^{2+}, \text{Co}^{2+}, \text{Ni}^{2+}, \text{Cu}^{2+}, \text{Zn}^{2+}, \text{Cd}^{2+}$) has been analyzed by many research groups [1–3]. $\text{Ca}_5\text{Mg}_3\text{Zn}(\text{VO}_4)_6$ was first characterized as a garnet having the crystal symmetry of space group $I\bar{4}3d$ [4]. The lattice comprises the VO_4 tetrahedra sharing edges with deformed CaO_8 dodecahedrons. The crystal structure of most of garnet-related vanadates is described with the symmetry of space group $Ia\bar{3}d$ [1]. These compounds attract increasing attention due to a cation deficiency, where the vacancy concentration in A position varies from 1/10 to 3/10 [5–8]. The nonstoichiometry values in B position were evaluated for $\text{Ca}_5\text{Co}_4(\text{VO}_4)_6$ [9].

Inorganic materials based on calcium vanadates have been studied as a new series of low-temperature co-fired ceramics [3] with promising microwave characteristics

below 100 °C [10–14]. The optical and photophysical properties of compounds doped with In, Ta [15], and lanthanide ions [16–18] have been considered in view of their application in solid-state lighting. $\text{Ca}_5\text{Mg}_4(\text{VO}_4)_6$ is characterized by cationic transport [19], whereas the vanadates $\text{Ca}_5\text{Mg}_{4-x}\text{Co}_x(\text{VO}_4)_6$ ($1 \leq x \leq 4$) demonstrate predominantly electronic conductivity about $10^{-2} \text{ S}\cdot\text{cm}^{-1}$ at 850 °C [20].

Different chemical routes are used to synthesize vanadates as single crystals as well and in polycrystalline forms [11–14, 20, 21]. Among them, solid-state method can be carried out in a quartz ampule upon annealing at 975 °C [4]. The melting point of V_2O_5 is, nevertheless, about 650 °C, and, typically, vanadium oxide melt interacts with quartz. Some single-crystal fiber methods are also employed for preparation of calcium vanadates [22, 23]. However, most of the approaches for the synthesis of target compounds of this class of inorganic solids are highly time-consuming and require special equipment. The widely reported method implies a solid-state reaction [24–26]. For example, the synthesis of $\text{Ca}_5\text{M}_4(\text{VO}_4)_6$ ($\text{M} = \text{Mg}$ and Zn) can be done taking MgCO_3 , ZnO , CaCO_3 and either NH_4VO_3 , or V_2O_5 as initial reagents with further annealing of the reaction mixture at 800–850 °C. The attempt to obtain $\text{Ca}_5\text{Zn}_{4-x}\text{Mg}_x(\text{VO}_4)_6$ ($0 \leq x \leq 3$) via a solid-state reaction results in the appearance

of ZnO as a second phase [10]. The problems of synthesis of the single-phase powders are reported not only for the above-mentioned system but for other compositions of garnet-type vanadates [1, 27, 28].

Wet-chemical synthesis procedure provides high homogeneity of its products [29, 30]. Many modified sol-gel methods using the corresponding nitrates as initial reagents are often applied to prepare vanadate-based solid solutions [15, 31, 32]. Other changes in the chemical routes to synthesize different inorganic solids include also mechanochemical treatment, variation of educts and raw materials, additional intermediate grindings and heat treatments, alternation in temperature of annealing. The observations listed above forces us to pay more attention to phase formation of the vanadate subclass of inorganic compounds. This can be accompanied by possible vaporization of vanadium oxides [33]. $\text{Ca}_5\text{Mg}_{4-x}\text{Zn}_x(\text{VO}_4)_6$ ($0 \leq x \leq 4$) is chosen as a model solid solution among garnet-related vanadates. Differential scanning calorimetry (DSC) analysis supplemented by gas emission analysis, *in situ* X-ray diffraction and evaluation of the local structure employing vibrational spectroscopy facilitate the solution of the problems in chemistry of vanadate-based materials more comprehensively than was reported earlier [4, 5, 10, 20, 31, 32]. The present study is also relevant to understanding of the synthesis processes of other garnet-type compounds such as silicates, hafnates, zirconates, germanates, etc.

2. Experimental

2.1. Reagents

The target ceramic samples of $\text{Ca}_5\text{Mg}_{4-x}\text{Zn}_x(\text{VO}_4)_6$ ($0 \leq x \leq 4$) were synthesized via a salt decomposition reaction using CaCO_3 (99%), MgCO_3 (99.999%), ZnO (99%), V_2O_5 (99.999%) or NH_4VO_3 (98%), HCOOH (98%, concentration 99%) and $\text{C}_6\text{H}_8\text{O}_7 \cdot \text{H}_2\text{O}$ (99%) as initial reagents. Those taken in a stoichiometric ratio were dissolved in distilled water with HCOOH . Ethanol was used as a grinding medium. Next, $\text{C}_6\text{H}_8\text{O}_7 \cdot \text{H}_2\text{O}$ was added with subsequent stirring and heating at 70–80 °C on a hot plate. Homogeneous water reagent solutions were slowly evaporated into a gel, which then formed a dry residue.

2.2. *In situ* synthesis

DSC and thermal gravimetric analysis (TG) were performed to estimate the optimal temperature of heat treatment of the final product. Thermal analysis was conducted with a Netzsch STA 449C Jupiter simultaneous analyzer operating with the heating rate of 10 K/min. *In situ* phase formation was studied by collecting of the X-ray powder diffraction (XRPD) patterns upon heating of the reagents $5\text{CaO}:4\text{MgO}:3\text{V}_2\text{O}_5$ and $5\text{CaO}:4\text{ZnO}:3\text{V}_2\text{O}_5$ taken with the stoichiometric ratios. Room temperature XRPD patterns before heating and after the phase formation were recorded using a Shimadzu XRD-7000 Maxima diffractometer and $\text{Cu K}\alpha$ radiation in the 2θ range between

10° and 90° . High temperature (HT) XRPD in the 2θ range between 15° and 60° was employed with Ni-filter instead of a graphite monochromator and a Shimadzu HA-1001 sample heating attachment (the scanning rate $1^\circ/\text{min}$; the 2θ step of 0.02°). The temperature uncertainty was maintained at less than 1°C . The xerogels obtained during the HT XRPD experiments were placed on a Pt plate. The samples were heated from 20°C up to 700°C at the rate $<10^\circ\text{C}/\text{min}$. Further heating was carried out from 700°C to 785°C in the steps of 15°C and the rate $<5^\circ\text{C}/\text{min}$. The samples were maintained for 1 h prior to every measurement at the temperatures listed. Heat treatment at 785°C was continued for over 12 h. Further heating was carried out on MgO -containing sample from 850°C to 950°C with the step 50°C and the rate $<5^\circ\text{C}/\text{min}$ with the dwell time of 1 h at every step. The scanning temperatures were selected according to the DSC curves of the precursor samples. The highest scanning temperature (820°C) was chosen for $\text{Ca}_5\text{Zn}_4(\text{VO}_4)_6$.

2.3. Characterization

XRPD patterns were collected at room temperature using a Rigaku DMAX-2200 diffractometer operating with $\text{Cu K}\alpha_1$ radiation over the angular range $15^\circ \leq 2\theta \leq 80^\circ$ with the step increment $\Delta 2\theta = 0.02^\circ$. The XRPD patterns were compared with those in the ICSD-Web database (2021). Rietveld refinement of the crystal structures was performed using the XRPD data collected on a Bruker D8 ADVANCE diffractometer with position-sensitive detector VÅNTEC-1 operating with $\text{Cu K}\alpha_1$ radiation (the angular range $10^\circ \leq 2\theta \leq 134^\circ$; the step increment $\Delta 2\theta = 0.021^\circ$). The XRPD patterns were compared with those in the PDF4+ICDD (2018) [34]. The crystallographic computing system JANA2006 [35] was employed for Rietveld refinements (Figs. S1–S5). Raman spectra were recorded on a Renishaw Ramascope U1000. This setup comprised a confocal Leica DML microscope, $50\times$ Olympus objective lens (the numerical aperture of 0.55), a notch filter, and a cooled charge-coupled device detector. A Renishaw HeNe laser operating at 632.8 nm and 4 mW at the sample was employed as an excitation source. Typical spectra acquisition time was 300 s and the resolution was 1 cm^{-1} . The Raman spectrum of silica was used for spectral calibration. Fourier transform infrared (FTIR) measurements were carried out on a Bruker vacuum spectrometer Tensor 27 using KBr pellets. The FTIR spectra were collected in a transmittance mode in the range from 400 cm^{-1} to 1000 cm^{-1} with the resolution of 2 cm^{-1} . The FTIR spectra in the range of $50\text{--}600\text{ cm}^{-1}$ were recorded using ATR technique with a diamond optical element employed at a Bruker Vertex 70v spectrometer. Vibrational spectroscopy was performed at room temperature.

3. Results and Discussion

Decomposition of the precursor colloidal solution upon heating in air is an exothermic process with the mass loss

mainly between 200 °C and 730 °C (Fig. 1). The total mass loss of the precursor mixture of $\text{Ca}_5\text{Mg}_4(\text{VO}_4)_6$ is 61.02 wt%, whereas the value of 52.57 wt% was obtained in the case of $\text{Ca}_5\text{Zn}_4(\text{VO}_4)_6$ up to 730 °C. Following the DSC data of a dried mixture of reagents, one can observe the water desorption at ~220 °C (Fig. 1) with the maximum of the DSC signal at 250 °C. It is accompanied by emission of CO_2 and NO_2 after decomposition of organics and $(\text{HN}_4)^-$ groups with energy uptake. The slow exothermal process at 270 °C associated with the prolonged emission of H_2O , CO_2 , NO_2 and NO was reported in earlier papers [31]. However, the next stages depicted in the DSC plots differ due to the other precursors chosen for synthesis. At 350 °C, there is an exothermal stage with the ongoing emission of the gases listed above (CO_2 and NO_2). After the known exothermal effect at 372 °C [31], a well pronounced exothermal peak near 450 °C correlates with emission of CO_2 , NO_2 and H_2O . This can evidently be explained by the exhaust that forms during the decomposition of the available organic matrix. The energy output at 510–528 °C is accompanied by emission of CO_2 , NO and NO_2 . Extraction of CO_2 and NO_2 occurs up to 730 °C with energy consumption. The observed disagreement between the obtained results and those reported earlier [31] arises from two main reasons. First, this difference may be caused by the reactants used to synthesize the target compositions. Second, the DSC data are analyzed in this study, whereas only the DTA results were presented previously [31]. The DSC curves of the dried precursor of $\text{Ca}_5\text{Zn}_4(\text{VO}_4)_6$ demonstrate several exothermal peaks at 396 °C, 451 °C, 528 °C and 727 °C and one endothermal one at 689.5 °C (Fig. 1). Some of the processes listed above can be evaluated more accurately employing *in situ* X-ray diffraction as an additional method.

The XRPD patterns of dried sol-gel precursors show the phase formation of CaCO_3 at 360 °C which is stable up to 785 °C (Fig. 2 and 3). Its appearance is accompanied by the emission of CO_2 from the decomposition of an organic matrix. The pyrovanadates CaMgV_2O_7 and $\text{Mg}_2\text{V}_2\text{O}_7$ are formed at 360 °C along with calcium carbonate (Fig. 2). The exothermal process near 450 °C is assigned to the formation of the intermediates $\alpha\text{-Zn}_2\text{V}_2\text{O}_7$ and $\text{Ca}_2\text{V}_2\text{O}_7$

whose crystal structures are characterized by monoclinic symmetry (Fig. 1–3). The energy output at 510 °C (or 566 °C in Ref. [31]) corresponds to the phase with a cubic structure (space group $1a\bar{3}d$). Extraction of CO_2 observed up to 730 °C with energy consumption is caused by the start of calcite decomposition, which ends at 785 °C, according to the XRPD data (Fig. 1–3).

The mixture of phases is observed from 460 °C to 950 °C in the magnesium-containing powder sample (Fig. 2), whereas the zinc-containing sample is characterized by coexistence of the phases like CaCO_3 , pyrovanadates, garnet-type vanadate in the temperature range 460–820 °C (Fig. 3).

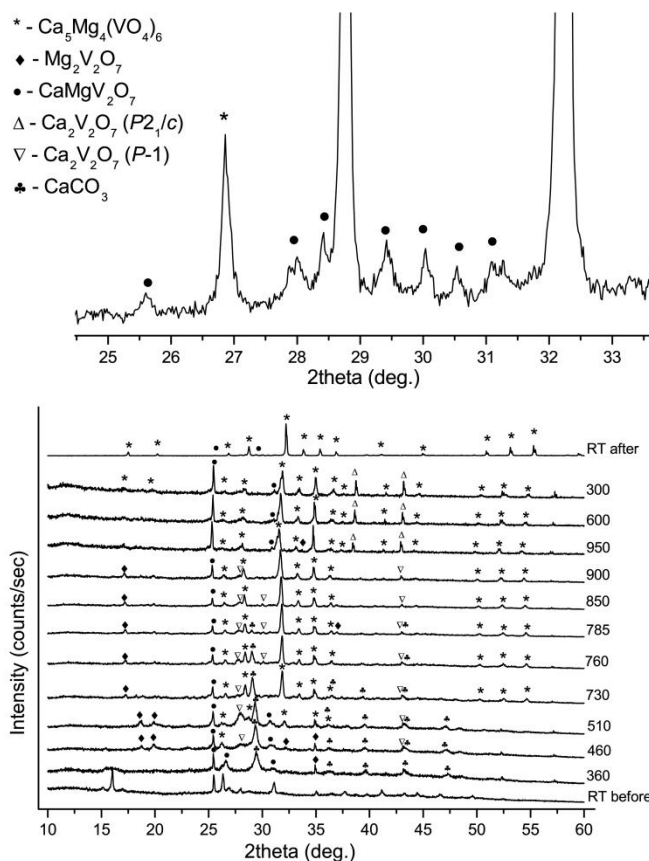


Fig. 2 HT XRPD profiles of $\text{Ca}_5\text{Mg}_4(\text{VO}_4)_6$ prepared via a sol-gel process: * - $\text{Ca}_5\text{Mg}_4(\text{VO}_4)_6$, ◆ - $\text{Mg}_2\text{V}_2\text{O}_7$, ● - CaMgV_2O_7 , Δ - $\text{Ca}_2\text{V}_2\text{O}_7$ ($P2_1/c$), ▽ - $\text{Ca}_2\text{V}_2\text{O}_7$ ($P1$), ♣ - CaCO_3

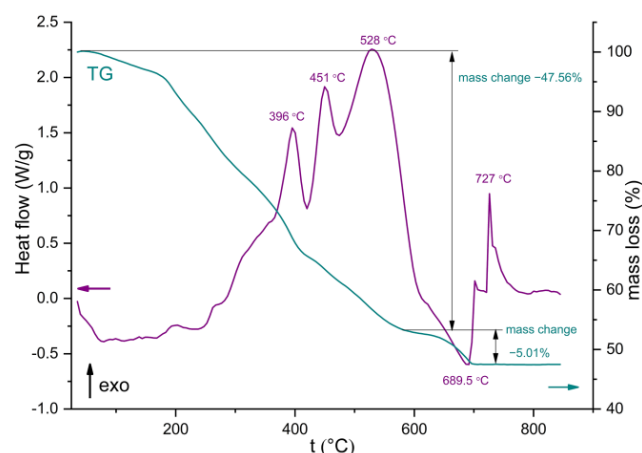
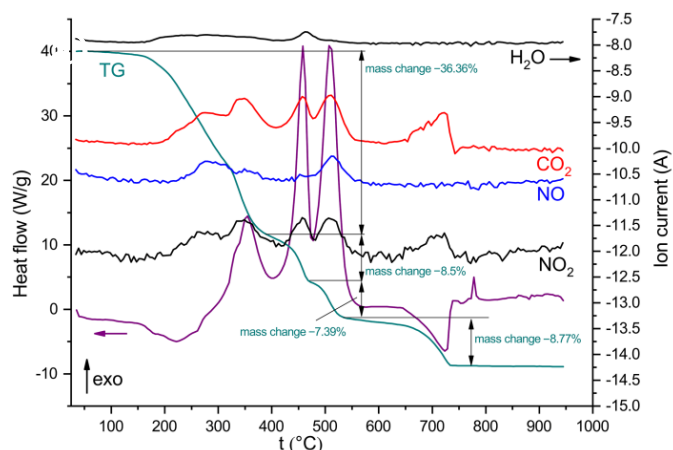


Fig. 1 DSC and TG curves with mass spectrometry analysis of the gaseous phase during heating of the xerogel powders $\text{Ca}_5\text{Mg}_4(\text{VO}_4)_6$ (left) and $\text{Ca}_5\text{Zn}_4(\text{VO}_4)_6$ (right) prepared by the sol-gel process

In turn, the phase transition in $\text{Zn}_2\text{V}_2\text{O}_7$ implies the change of space group $C2/c \rightarrow C2/m$ at 620 °C [36]. $\text{Ca}_2\text{V}_2\text{O}_7$ undergoes also the phase transition $P\bar{1} \rightarrow P2_1/c$ above 900 °C. CaMgV_2O_7 melts incongruently at 885 °C, whereas $\text{Ca}_2\text{V}_2\text{O}_7$ and $\text{Mg}_2\text{V}_2\text{O}_7$ are thermally stable even at 950 °C.

The coexistence of $\text{Ca}_5\text{Mg}_4(\text{VO}_4)_6$ (space group $Ia\bar{3}d$) and CaMgV_2O_7 (space group $P2_1/c$) is detected at room temperature in the reaction products (Fig. 2). In this way, one can carry out synthesis at 850 °C and, after short-term heat treatment, can obtain the target product with contamination of $\text{Ca}_2\text{V}_2\text{O}_7$. The presence of satellite pyrovanadate phases was revealed in many earlier studies on evaluation of the most efficient chemical route to synthesize garnet-type vanadates [3, 5, 15]. The elimination of these satellite pyrovanadates is a complex problem which is often dismissed when the target chemical products of $\text{Ca}_5\text{M}_4(\text{VO}_4)_6$ ($M = \text{Mg}, \text{Zn}, \text{Co}, \text{etc.}$) are synthesized. Fortunately, the impurity-free samples can be obtained. However, this usually requires a long duration of thermal treatment [4, 5]. Indeed, the heat treatment at 980 °C for 150 h allows a single-phase sample of $\text{Ca}_5\text{Mg}_4(\text{VO}_4)_6$ to be prepared. This temperature of the final annealing during the synthesis procedure corresponds to the melting point of $\text{Mg}_2\text{V}_2\text{O}_7$.

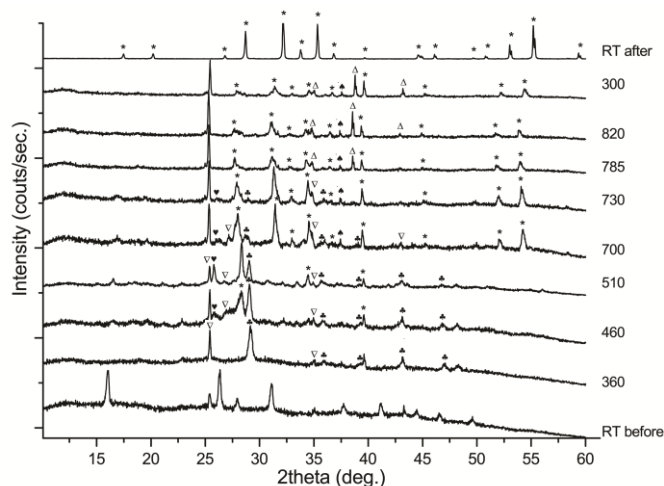


Fig. 3 HT XRPD profiles of $\text{Ca}_5\text{Zn}_4(\text{VO}_4)_6$ prepared via a sol-gel process: * - $\text{Ca}_5\text{Zn}_4(\text{VO}_4)_6$, Δ - $\text{Ca}_2\text{V}_2\text{O}_7$ ($P2_1/c$), ∇ - $\text{Ca}_2\text{V}_2\text{O}_7$ ($P\bar{1}$), \clubsuit - CaCO_3 , \heartsuit - $\alpha\text{-Zn}_2\text{V}_2\text{O}_7$, \spadesuit - $\beta\text{-Zn}_2\text{V}_2\text{O}_7$

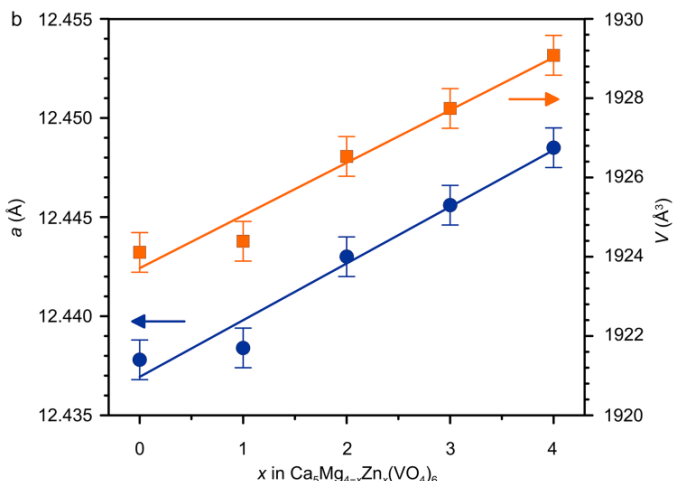
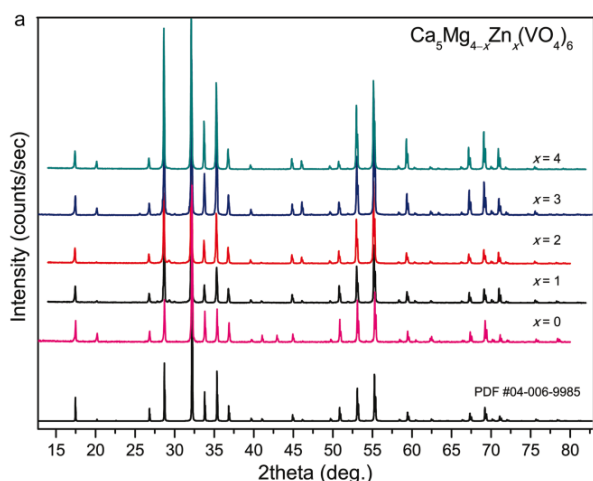


Fig. 4 XRPD patterns of $\text{Ca}_5\text{Mg}_{4-x}\text{Zn}_x(\text{VO}_4)_6$ ($0 \leq x \leq 4$) (a), concentration dependence of the lattice parameters in $\text{Ca}_5\text{Mg}_{4-x}\text{Zn}_x(\text{VO}_4)_6$ ($0 \leq x \leq 4$) (b)

The XRPD analysis shows that polycrystalline $\text{Ca}_5\text{Mg}_{4-x}\text{Zn}_x(\text{VO}_4)_6$ ($0 \leq x \leq 4$) with some quantity (2–3 wt%) of pyrovanadate phases is formed via the sol-gel process (Fig. 4). The crystal structures of $\text{Ca}_5\text{Mg}_{4-x}\text{Zn}_x(\text{VO}_4)_6$ ($0 \leq x \leq 4$) were refined using the Rietveld method (Table S1; Supporting Information). The solid solution $\text{Ca}_5\text{Mg}_{4-x}\text{Zn}_x(\text{VO}_4)_6$ ($0 \leq x \leq 4$) crystallizes in the cubic space group $Ia\bar{3}d$, $Z = 8$ (Supporting Information: Fig. S1–S5). The fractional atomic coordinates and refinement parameters are listed in Table 1. Magnesium and zinc cations have close radii that promotes the formation of solid solutions [38]. Both Mg and Zn ions occupy the octahedral position (16a) and the formation of the solid solutions is proved by a linear change in the cell parameter and volume when zinc concentration increases (Fig. 4). The lattice parameter a refined for $\text{Ca}_5\text{Mg}_3\text{Zn}(\text{VO}_4)_6$ deviates from the linear dependence because of a relatively large amount of CaMgV_2O_7 impurity (Supporting Information: Table S1).

The site occupancy factor of Ca^{2+} positions is chosen to be about 5/6 that is close to the data reported by Ronniger and Mill [6]. Cation deficiency from 1/10 to 3/10 is not surprising and was also observed in other garnet-type vanadates [6, 39]. Therefore, a study of the local structure of these compounds becomes highly relevant in view of high deficiency in the cation sublattice.

Eight molecules of $\text{Ca}_2.5\text{M}^{\text{II}}_2(\text{VO}_4)_3$ ($\text{M}^{\text{II}} = \text{Mg}, \text{Zn}$) per primitive cell in the $Ia\bar{3}d$, (O_h^{10}) structure support $3 \times 8 \times 19.5 = 468$ modes of vibration with $K=0$ involving the zero-frequency translational motion of the crystal. These vibrations are classified according to irreducible representations of the point group of the elementary cell [40]. Given that the number of equivalent sites in any set is defined by the order of the point group divided by the order of the site symmetry subgroup for the primitive or primitive rhombohedral lattices, the number is greater for the centered lattices. The body-centered unit cells have twice as many points as the primitive ones (Table 1).

The vibration modes of the full symmetry group are characterized by the following irreducible representations of O_h

$$\Gamma^{cryst} = 3A_{1g} + 5A_{1u} + 5A_{2g} + 5A_{2u} + 8E_g + 10E_u + 13F_{1g} + 18F_{1u} + 14F_{2g} + 15F_{2u} \quad (1)$$

Three acoustic modes are described by $\Gamma^{acoust} = F_{1u}$ and the remaining ones,

$$\Gamma_{vib}^{cryst} = 3A_{1g} + 5A_{1u} + 5A_{2g} + 5A_{2u} + 8E_g + 10E_u + 13F_{1g} + 17F_{1u} + 14F_{2g} + 15F_{2u}, \quad (2)$$

correspond to the optical modes, among which A_{1u} , A_{2g} , A_{2u} , E_u , F_{1g} and F_{2u} are inactive. The modes of the F_{1u} sym-

metry are infrared active and the combination of A_{1g} , E_g and F_{2g} is Raman active. Infrared and Raman activities are presented in Table 2.

Vibrational modes can be classified in two main categories [41, 42], i.e., internal modes of the tetrahedral VO_4 unit with the molecular symmetry S_4 and external modes, which include translations of Ca^{2+} , Mg^{2+} , Zn^{2+} and $[VO_4]^{3-}$ ions, and librations of $[VO_4]^{3-}$. In a lattice of $A_{2.5}B_2(VO_4)_3$, zone-center Raman active vibrational modes can be distinguished for Ca^{2+} cations (A-site in $A_{2.5}B_2(VO_4)_3$) and VO_4 tetrahedra, whereas Mg^{2+}/Zn^{2+} cations (B-site) do not produce Raman active vibrations.

Table 1 Fractional atomic coordinates and isotropic thermal displacement parameters (B) of $Ca_5Mg_{4-x}Zn_x(VO_4)_6$, $0 \leq x \leq 4$ (SG $Ia\bar{3}d$, $Z = 8$)

Atom	Wyckoff position	x	y	z	SOF*	B
		$Ca_5Mg_4(VO_4)_6$		$R_{wp} = 0.112, R_p = 0.062, GOF = 0.058$		
Ca	24c	0.125	0	0.25	0.83	0.68(5)
Mg	16a	0	0	0	1.00	0.10(4)
V	24d	0.375	0	0.25	1.00	0.18(3)
O	96h	0.0980(2)	0.2001(1)	0.2887(1)	1.00	0.67(7)
		$Ca_5Mg_3Zn(VO_4)_6$		$R_{wp} = 0.163, R_p = 0.099, GOF = 0.041$		
Ca	24c	0.125	0	0.25	0.83	0.10(4)
Mg/Zn	16a	0	0	0	0.75/0.25	0.57(5)
V	24d	0.375	0	0.25	1.00	0.10(3)
O	96h	0.0938(3)	0.2032(1)	0.2896(1)	1.00	0.39(6)
		$Ca_5Mg_2Zn_2(VO_4)_6$		$R_{wp} = 0.128, R_p = 0.086, GOF = 0.020$		
Ca	24c	0.125	0	0.25	0.83	0.51(6)
Mg/Zn	16a	0	0	0	0.5/0.5	0.09(3)
V	24d	0.375	0	0.25	1.00	0.20(4)
O	96h	0.0961(2)	0.1966(2)	0.2879(2)	1.00	0.58(8)
		$Ca_5MgZn_3(VO_4)_6$		$R_{wp} = 0.162, R_p = 0.089, GOF = 0.037$		
Ca	24c	0.125	0	0.25	0.83	0.16(2)
Mg/Zn	16a	0	0	0	0.25/0.75	0.30(4)
V	24d	0.375	0	0.25	1.00	0.25(3)
O	96h	0.0929(2)	0.1969(1)	0.2891(1)	1.00	0.40(6)
		$Ca_5Zn_4(VO_4)_6$		$R_{wp} = 0.142, R_p = 0.078, GOF = 0.045$		
Ca	24c	0.125	0	0.25	0.83	0.63(2)
Zn	16a	0	0	0	1.00	0.22(1)
V	24d	0.375	0	0.25	1.00	0.10(2)
O	96h	0.0955(5)	0.1977(3)	0.2885(1)	1.00	0.73(4)

* SOF stands for site occupancy factor

Table 2 Classification of the $k = 0$ unit cell modes* for $Ca_{2.5}M^{II}_2(VO_4)_3$, $M^{II} = Mg, Zn$ (SG $Ia\bar{3}d$, $Z = 8$)

Factor group O_h	Lattice modes			Internal modes $[VO_4]^{3-}$	Selection rules	
	Acoustic	Librational	Translational		infrared	Raman
A_{1g}		1		2		$xx + yy + zz$
A_{1u}			2	3		
A_{2g}			2	3		
A_{2u}		1	2	2		
E_g		1	2	5		$xx + yy + 2zz,$ $\sqrt{3}xx - \sqrt{3}yy$
E_u		1	4	5		
F_{1g}		3	4	6		
F_{1u}	1	2	8	7	T	
F_{2g}		2	5	7		xy, yz, xz
F_{2u}		3	6	6		
Overall	3	36	87	108	$\Sigma = 234$	

* The F_{1u} modes are infrared and the A_{1g} , E_g and F_{2g} modes are Raman active.

Translations and librations of the VO_4 unit are associated with the representations below:

$$T'(\text{VO}_4) = A_{1u} + A_{2g} + E_g + E_u + 2F_{1g} + 3F_{1u} + 3F_{2g} + 2F_{2u} \quad (3)$$

$$L(\text{VO}_4) = A_{1g} + A_{2u} + E_g + E_u + 3F_{1g} + 2F_{1u} + 2F_{2g} + 3F_{2u} \quad (4)$$

Once acoustic modes are subtracted, the external modes are distributed among the irreducible representation $A_{1g} + 2A_{1u} + 2A_{2g} + 3A_{2u} + 3E_g + 5E_u + 7F_{1g} + 10F_{1u} + 7F_{2g} + 9F_{2u}$. Therefore, the internal modes of the tetrahedral VO_4 unit can be characterized by

$$\Gamma_{vib}^{cryst} = 2A_{1g} + 3A_{1u} + 3A_{2g} + 2A_{2u} + 5E_g + 5E_u + 6F_{1g} + 7F_{1u} + 7F_{2g} + 6F_{2u} \quad (5)$$

In $\text{Ca}_{2.5}\text{M}^{\text{II}}_2(\text{VO}_4)_3$ ($\text{M}^{\text{II}} = \text{Mg}, \text{Zn}$), the symmetry of the VO_4 tetrahedron changes due to the site symmetry and crystal field effects, and all the internal modes are split. The latter are summarized in Table 3.

FTIR and Raman spectroscopy techniques are employed to study possible structural changes when Mg^{2+} cations are substituted for Zn^{2+} in the solid solution $\text{Ca}_5\text{Mg}_{4-x}\text{Zn}_x(\text{VO}_4)_6$. Both types of vibrational spectra of $\text{Ca}_5\text{Mg}_{4-x}\text{Zn}_x(\text{VO}_4)_6$ ($0 \leq x \leq 4$) are similar and do not indicate any significant changes in the crystal structure (Fig. 5). Whereas 25 Raman and 17 infrared modes are active according to the group theory, not all of them can actually be detected [10]. This discrepancy originates from the negligible changes in polarizability and dipole moment, which do not give rise to observable Raman and infrared modes [43]. According to the previous studies on garnet compounds [41, 44, 45], the Raman lines between 910 cm^{-1} and 950 cm^{-1} and infrared bands in the range of $700\text{--}950 \text{ cm}^{-1}$ correspond to the internal anti-symmetric (ν_3) stretching vibrations of $[\text{VO}_4]^{3-}$ ions, whereas the symmetric (ν_1) stretching modes of $[\text{VO}_4]^{3-}$ are revealed only in the Raman spectra between 690 cm^{-1} and 875 cm^{-1} . Typical weak Raman lines at $\sim 450 \text{ cm}^{-1}$ with the shoulder at $\sim 430 \text{ cm}^{-1}$ are expected for the VO_4 bending vibrations. An observed general order of mode frequencies, i.e., $L(\text{VO}_4) > T'$ (the metal cation) $> T'(\text{VO}_4)$ is also presented in most garnet-type silicates. A very strong Raman peak (as well as some weak ones) at $\sim 320 \text{ cm}^{-1}$ is attributed to the librational VO_4 modes which can be also distinguished as the infrared band in the range of $340\text{--}380 \text{ cm}^{-1}$ (Fig. 5).

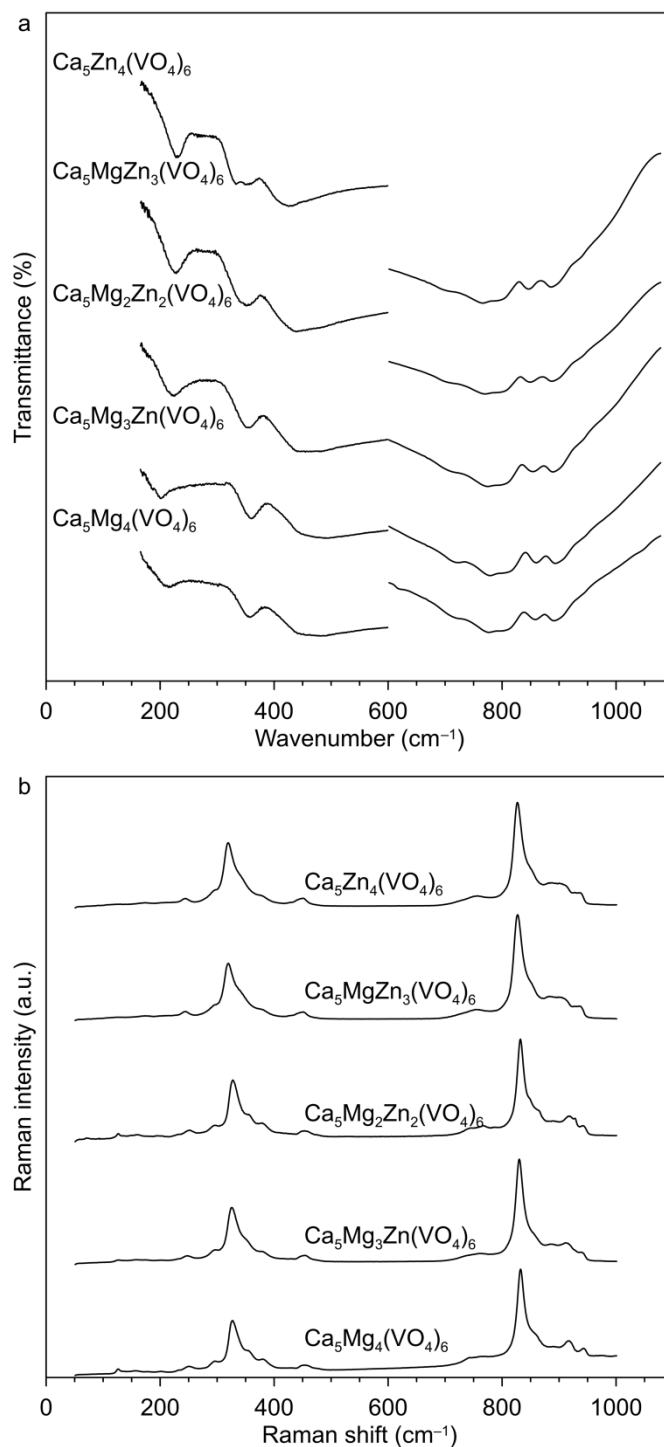


Fig. 5 Infrared (a) and Raman (b) spectra of $\text{Ca}_5\text{Mg}_{4-x}\text{Zn}_x(\text{VO}_4)_6$ ($0 \leq x \leq 4$)

Table 3 Correlation table for the internal vibrations of $[\text{VO}_4]^{3-}$ in $\text{Ca}_{2.5}\text{M}^{\text{II}}_2(\text{VO}_4)_3$, $\text{M}^{\text{II}} = \text{Mg}, \text{Zn}$ (SG $Ia\bar{3}d$, $Z = 8$)

$[\text{VO}_4]^{3-}$ site symmetry and factor group	Normal modes of free $[\text{VO}_4]^{3-}$ with T_d symmetry			
	$\nu_1 (A_1)$	$\nu_2 (E)$	$\nu_3 (F_2)$	$\nu_4 (F_2)$
	Splitting of normal modes of T_d symmetry due to site symmetry and factor group effects			
S_4	A	$A + B$	$B + E$	$B + E$
O_h	$A_{1g} + A_{2u} + E_g + E_u + F_{1g} + F_{2u}$	$A_{1g} + A_{1u} + A_{2g} + A_{2u} + 2E_g + 2E_u + F_{1g} + F_{1u} + F_{2g} + F_{2u}$	$A_{1u} + A_{2g} + E_g + E_u + 2F_{1g} + 3F_{1u} + 3F_{2g} + 2F_{2u}$	$A_{1u} + A_{2g} + E_g + E_u + 2F_{1g} + 3F_{1u} + 3F_{2g} + 2F_{2u}$

The Raman line at $\sim 245\text{ cm}^{-1}$ is assigned to translation modes of Ca^{2+} . Meanwhile, $T'(\text{Ca}^{2+})$ and $T'(\text{Mg}^{2+}/\text{Zn}^{2+})$ modes are associated with the infrared band at $190\text{--}250\text{ cm}^{-1}$. Very weak Raman lines below 200 cm^{-1} correspond to external translations of VO_4 tetrahedrons. The latter stand in the line with the $T'(\text{SiO}_4)$ modes analyzed previously for $\text{A}_3\text{B}_2(\text{SiO}_4)_3$ ($\text{A} = \text{Mg, Ca, Mn, Fe}$; $\text{B} = \text{Al, Cr, Fe}$) [44, 45]. Substitution of Mg^{2+} by Zn^{2+} in $\text{Ca}_5\text{Mg}_{4-x}\text{Zn}_x(\text{VO}_4)_6$ leads to the monotonic increase of the unit cell parameter (Fig. 4b) and a slight shift (not exceeding $\sim 10\text{ cm}^{-1}$) of most of the vibrational bands towards lower wavenumbers (Fig. 5). The similar dependencies of vibrational frequencies on the lattice parameter were earlier found in silicate garnets [44, 45]. Given that the density of modes is relatively high to allow a clear assignment of all the lines, it is obviously not complete. Therefore, first-principle calculations in the density functional theory (DFT) framework based on the geometry optimization of $\text{Ca}_5\text{M}_4(\text{VO}_4)_6$ ($\text{M} = \text{Mg, Zn}$) are needed to perform an accurate assignment of vibrational bands and will be discussed elsewhere.

4. Conclusions

High-temperature X-Ray diffraction supported by DSC technique allowed studying $\text{Ca}_5\text{Mg}_{4-x}\text{Zn}_x(\text{VO}_4)_6$ ($0 \leq x \leq 4$) so as to provide more detailed and reliable data on the phase formation of garnet-type vanadates. The synthesis of Zn-doped $\text{Ca}_5\text{Mg}_4(\text{VO}_4)_6$ is accompanied by the appearance of $\text{Ca}_2\text{V}_2\text{O}_7$, $\text{Mg}_2\text{V}_2\text{O}_7$ or $\text{Zn}_2\text{V}_2\text{O}_7$. These satellite pyrovanadate phases are stable up to $950\text{ }^\circ\text{C}$ and disappear only above their melting point. The single-phase samples of $\text{Ca}_5\text{Mg}_4(\text{VO}_4)_6$ and $\text{Ca}_5\text{Zn}_4(\text{VO}_4)_6$ can be obtained following heat treatment for 150 h at $980\text{ }^\circ\text{C}$ and at $750\text{ }^\circ\text{C}$, respectively. The formation of the solid solution $\text{Ca}_5\text{Mg}_{4-x}\text{Zn}_x(\text{VO}_4)_6$ ($0 \leq x \leq 4$) was confirmed by XRPD and vibrational spectroscopy. The findings in structural chemistry contribute to understanding of the impact of synthesis procedures on crystal engineering of vanadates and other garnet-type oxides.

Supplementary materials

Supplementary materials in the online format are available at the website of this paper. These data contain:

Table S1: Phase composition and lattice parameters of $\text{Ca}_5\text{Mg}_{4-x}\text{Zn}_x(\text{VO}_4)_6$ ($0 \leq x \leq 4$). **Fig. S1:** Rietveld refinement of $\text{Ca}_5\text{Mg}_4(\text{VO}_4)_6$ from XRPD data. **Fig. S2:** Rietveld refinement of $\text{Ca}_5\text{Mg}_3\text{Zn}(\text{VO}_4)_6$ from XRPD data. **Fig. S3:** Rietveld refinement of $\text{Ca}_5\text{Mg}_2\text{Zn}_2(\text{VO}_4)_6$ from XRPD data. **Fig. S4:** Rietveld refinement of $\text{Ca}_5\text{MgZn}_3(\text{VO}_4)_6$ from XRPD data. **Fig. S5:** Rietveld refinement of $\text{Ca}_5\text{Zn}_4(\text{VO}_4)_6$ from XRPD data.

Funding

This study was funded by the Research Programs No. AAAA-A19-119020190042-7 and No. AAAA-A19-119020190044-1 (IHTE UB RAS).

Acknowledgments

We are grateful to Dr. Olga G. Reznitskikh (ISSC UB RAS), Dr. Elena A. Sherstobitova (IMP UB RAS) and Dr. Nikolai I. Moskalenko (IHTE UB RAS) for technical assistance. The crystallographic and spectroscopic studies were carried out in the Shared Access Centers at IMET UB RAS and IHTE UB RAS, respectively.

Author contributions

Conceptualization: A.S.T.
Data curation: I.I.L., A.S.T.
Formal Analysis: S.A.P., O.M.F., I.I.L.
Funding acquisition: I.I.L., A.S.T.
Methodology: S.N.S.
Project administration: A.S.T.
Resources: S.G.T.
Supervision: S.G.T., S.N.S.
Validation: S.N.S.
Visualization: I.I.L., A.S.T.
Writing – original draft: A.S.T.
Writing – review & editing: I.I.L.

Conflict of interest

The authors declare no conflict of interest.

Additional information

Webpages of

Institute of High-Temperature electrochemistry:
http://www.ihte.uran.ru/?page_id=3106;

Institute of Metallurgy: <http://www.imet-uran.ru>.

References

1. Mill BV, Ronniger G, Kabalov YuK. New garnet compounds $\text{A}_3^{2+}\text{B}_2^{2+}\text{C}^{4+}\text{V}_2^{5+}\text{O}_{12}$ ($\text{A} = \text{Ca, Cd}$; $\text{B} = \text{Mg, Zn, Co, Ni, Cu, Mn, Cd}$; $\text{C} = \text{Ge, Si}$). Russ J Inorg Chem. 2014;59:1208–1213. doi:[10.1134/S0036023614110151](https://doi.org/10.1134/S0036023614110151)
2. Ishi K, Ikuta Y. Isomorphous substitutions in vanadate garnets. N Jb Miner Abh. 2006;182:157–163. doi:[10.1127/0077-7757/2006/0038](https://doi.org/10.1127/0077-7757/2006/0038)
3. Yao GG, Liu P, Zhang HW. Novel series of low-firing microwave dielectric ceramics: $\text{Ca}_5\text{A}_4(\text{VO}_4)_6$ ($\text{A}^{2+} = \text{Mg, Zn}$). J Am Ceram Soc 2013;96:1691–1693. doi:[10.1111/jace.12359](https://doi.org/10.1111/jace.12359)
4. Müller-Buschbaum Hk, von Postel M. Eine weitere Oxovanadat-Phase mit Granatstruktur: $\text{Ca}_5\text{Mg}_3\text{ZnV}_6\text{O}_{24}$. Z Anorg Allg Chem. 1992;615:101–103. doi:[10.1002/zaac.19926150920](https://doi.org/10.1002/zaac.19926150920)
5. Krasnenko TI, Zolotukhina LV, Zabolotskaya EV, Svetlakov SV, Dobosh VG. Defect structure and electrical and magnetic properties of calcium manganese vanadium garnets. Inorg Mater. 1999;35:1179–1182.

6. Ronniger G, Mill BV. Vanadates with a defect garnet structure. *Sov Phys Crystallogr.* 1973;18:303–307.
7. Surat LL, Fotiev AA, Dobosh VG. V_2O_5 -MgO-CaO-MnO(Mn_2O_3) system. *Zh. Neorg. Khim.* 1989;34:2924–2928.
8. Slobodin BV, Fotiev AA, Sharova NG. Phase composition of the CaO-MgO- V_2O_5 system. *Zh Neorg Khim.* 1977;23:184–187.
9. Li B, Zheng JG, Li W. Influence of cobalt ions non-stoichiometry on the microstructure and microwave properties of $Ca_5Co_4(VO_4)_6$ ceramics. *Ceram Int.* 2017;43:13956–13962. doi:[10.1016/j.ceramint.2017.07.127](https://doi.org/10.1016/j.ceramint.2017.07.127)
10. Li B, Tian J, Qiu L. Crystal structures and microwave dielectric properties of low-firing $Ca_5Zn_{4-x}Mg_xV_6O_{24}$ ceramics. *Ceram Int.* 2018;44:18250–18255. doi:[10.1016/j.ceramint.2018.07.035](https://doi.org/10.1016/j.ceramint.2018.07.035)
11. Wang D, Xiang HC, Tang Y, Fang L, Khaliq J, Li CC. A low-firing $Ca_5Ni_4(VO_4)_6$ ceramic with tunable microwave dielectric properties and chemical compatibility with Ag. *Ceram Int.* 2016;42:15094–15098. doi:[10.1016/j.ceramint.2016.06.085](https://doi.org/10.1016/j.ceramint.2016.06.085)
12. Fang L, Xiang F, Su CX, Zhang H. A novel low firing microwave dielectric ceramic $NaCa_2Mg_2V_3O_{12}$. *Ceram Int.* 2013;39:9779–9783. doi:[10.1016/j.ceramint.2013.05.041](https://doi.org/10.1016/j.ceramint.2013.05.041)
13. Xiang HC, Fang L, Jiang XW, Li CC. Low-firing and microwave dielectric properties of $Na_2YMg_2V_3O_{12}$ ceramic. *Ceram Int.* 2016;42:3701–3705. doi:[10.1016/j.ceramint.2015.10.163](https://doi.org/10.1016/j.ceramint.2015.10.163)
14. Yao GG, Liu P, Zhao XG, Zhou JP, Zhang HW. Low-temperature sintering and microwave dielectric properties of $Ca_5Co_4(VO_4)_6$ ceramics. *J Eur Ceram Soc.* 2014;34:2983–2987. doi:[10.1016/j.jeurceramsoc.2014.03.026](https://doi.org/10.1016/j.jeurceramsoc.2014.03.026)
15. Pavitra E, Raju GSR, Park JY, Wang L, Moon BK, Yu JS. Novel rare-earth-free yellow $Ca_2Zn_{3.92}In_{0.08}(V_{0.99}Ta_{0.01}O_4)_6$ phosphors for dazzling white light-emitting diodes. *Sci Rep.* 2015;5:10296. doi:[10.1038/srep10296](https://doi.org/10.1038/srep10296)
16. Li JF, Qiu KH, Li JF, Li W, Yang Q, Li JH. A novel broadband emission phosphor $Ca_2KMg_2V_3O_{12}$ for white light emitting diodes. *Mater Res Bull.* 2010;45:598–602. doi:[10.1016/j.materresbull.2010.01.014](https://doi.org/10.1016/j.materresbull.2010.01.014)
17. Song D, Guo CF, Zhao J, Suo H, Zhao XQ, Zhou XJ, Liu GZ. Host sensitized near-infrared emission in Nd^{3+} - Yb^{3+} Co-doped $Na_2GdMg_2V_3O_{12}$ phosphor. *Ceram Int.* 2016;42:12988–12994. doi:[10.1016/j.ceramint.2016.05.072](https://doi.org/10.1016/j.ceramint.2016.05.072)
18. Dhobale AR, Mohapatra M, Natarajan V, Godbole SV. Synthesis and photoluminescence investigations of the white light emitting phosphor, vanadate garnet, $Ca_2NaMg_2V_3O_{12}$ co-doped with Dy and Sm. *J Lumin.* 2012;132:293–298. doi:[10.1016/j.jlumin.2011.09.004](https://doi.org/10.1016/j.jlumin.2011.09.004)
19. Leonidova ON, Patrakeev MV, Leonidov IA. Ionic and electronic transport in the garnet-type vanadate $Ca_{2.5}Mg_2V_3O_{12}$. *J Solid State Electrochem.* 2019;23:1083–1088. doi:[10.1007/s10008-019-0420-y](https://doi.org/10.1007/s10008-019-0420-y)
20. Tolkacheva AS, Shkerin SN, Nikonov AV, Pershina SV, Khavlyuk PD, Leonidov II. Electrical and thermal properties of $Ca_5Mg_{4-x}Co_x(VO_4)_6$ ($0 \leq x \leq 4$), a promising electrode material. *Mater. Lett.* 2021;305:30811. doi:[10.1016/j.matlet.2021.130811](https://doi.org/10.1016/j.matlet.2021.130811)
21. Blanzat B, Loriers J. Synthèse et étude des propriétés spectrales de monocristaux de vanadate a structure grenat $Ca_2NaMg_2V_3O_{12}$ active par l'euporium trivalent. *Mater Res Bull.* 1974;9:1647–1654. doi:[10.1016/0025-5408\(74\)90156-1](https://doi.org/10.1016/0025-5408(74)90156-1)
22. Dhanaraj G, Byrappa K, Prasad V, Dudley M. (Eds.). Springer Handbook of Crystal Growth. Heidelberg, Germany: Springer-Verlag GmbH; 2010. 1736 p.
23. Yu YM, Chani VI, Shimamura K, Inaba K, Fukuda T. Growth of vanadium garnet fiber crystals and variations of lattice parameter. *J Cryst Growth* 1997;177:74–78. doi:[10.1016/S0022-0248\(97\)01070-1](https://doi.org/10.1016/S0022-0248(97)01070-1)
24. Levina AA, Tadevosyan NO, Petrova SA, Buyanova ES, Morozova MV. Phase formation processes and synthesis of solid solutions in Ca-R-Nb-M-O systems. *Chimica Techno Acta.* 2020;7:17–25. doi:[10.15826/chimtech.2020.7.1.03](https://doi.org/10.15826/chimtech.2020.7.1.03)
25. Klyndyuk AI, Chizhova EA, Shevchenko SV. Spin-state transition in the layered barium cobaltite derivatives and their thermoelectric properties. *Chimica Techno Acta.* 2020;7:26–33. doi:[10.15826/chimtech.2020.7.1.04](https://doi.org/10.15826/chimtech.2020.7.1.04)
26. Klyndyuk AI, Zhuravleva YY, Gundilovich NN. Crystal structure, thermal and electrotransport properties of $NdBa_{1-x}Sr_xFeCo_{0.5}Cu_{0.5}O_{5+8}$ ($0.02 \leq x \leq 0.20$) solid solutions. *Chimica Techno Acta.* 2021;8:20218301. doi:[10.15826/chimtech.2021.8.3.01](https://doi.org/10.15826/chimtech.2021.8.3.01)
27. Huang XY, Wang SY, Rtimi S, Devakumar B. $KCa_2Mg_2V_3O_{12}$: A novel efficient rare-earth-free self-activated yellow emitting phosphor. *J Photochem Photobiol A Chem.* 2020;401:112765. doi:[10.1016/j.jphotochem.2020.112765](https://doi.org/10.1016/j.jphotochem.2020.112765)
28. Tsirlin AA, Dikarev EV, Velikodny YA, Shpanchenko RV, Antipov EV. $Pb_{2.63}Cd_2V_3O_{12}$, a cation-deficient garnet-type vanadate. *Acta Crystallogr C Struct Chem.* 2007;63:140–142. doi:[10.1107/S0108270107021233](https://doi.org/10.1107/S0108270107021233)
29. Dutta U, Haque A, Seikh MM. Synthesis, structure and magnetic properties of Ti doped La_2MnNiO_6 double perovskite. *Chimica Techno Acta.* 2019;6:80–92. doi:[10.15826/chimtech.2019.6.3.01](https://doi.org/10.15826/chimtech.2019.6.3.01)
30. Anokhina IA, Animitsa IE, Buzina AF, Voronin VI, Vykhodets VB, Kurennykh TE, Zaikov YP. Synthesis, structure and electrical properties of Li^+ -doped pyrochlore $Gd_2Zr_2O_7$. *Chimica Techno Acta.* 2020;7:51–60. doi:[10.15826/chimtech.2020.7.2.02](https://doi.org/10.15826/chimtech.2020.7.2.02)
31. Park JY, Chung JW, Yang HK. Synthesis and photoluminescence properties of yellow-emitting $Ca_5(Zn_{1-x}Mg_x)_4(VO_4)_6$ self-activated phosphors. *Optik.* 2018;155:384–389. doi:[10.1016/j.ijleo.2017.11.046](https://doi.org/10.1016/j.ijleo.2017.11.046)
32. Tolkacheva AS, Shkerin SN, Zemlyanoi KG, Reznitskikh OG, Pershina SV, Khavlyuk PD. Thermal and electrical properties of $Ca_5Mg_{4-x}Zn_x(VO_4)_6$ ($0 \leq x \leq 4$). *J Therm Anal Calorim.* 2019;136:1003–1009. doi:[10.1007/s10973-018-7780-z](https://doi.org/10.1007/s10973-018-7780-z)
33. Lide DR. Handbook of Chemistry and Physics. 84th ed., Boca Raton, FL: CRC Press LLC; 2003. p. 4–93.
34. Powder Diffraction File PDF4+ ICDD 2018.
35. Petříček V, Dušek M, Palatinus L. Crystallographic computing system JANA2006: General features. *Z. Kristallogr.* 2014;229:345–352. doi:[10.1515/zkri-2014-1737](https://doi.org/10.1515/zkri-2014-1737)
36. Krasnenko TI, Zubkov VG, Tyutyunnik AP, Zolotukhina LV, Vasyutinskaya EF. Crystal structure of β' - $Zn_2V_2O_7$. *Crystallogr. Rep.* 2003;48:35–38. doi:[10.1134/1.1541739](https://doi.org/10.1134/1.1541739)
37. Miyauchi A, Okabe TH. Production of metallic vanadium by preform reduction process. *Mater Trans.* 2010;51(6):1102–1108. doi:[10.2320/matertrans.M2010027](https://doi.org/10.2320/matertrans.M2010027)
38. Shannon RD, Prewitt CT. Effective ionic radii in oxides and fluorides. *Acta Crystallogr B Struct Sci Cryst Eng Mater.* 1969;25:925–946. doi:[10.1107/S0567740869003220](https://doi.org/10.1107/S0567740869003220)
39. Fotiev AA. Vanadaty: Sostav, Sintez, Struktura, Svoistva [Vanadates: composition, synthesis, structure, properties] Moscow: Nauka; 1988. 272 p. Russian.
40. Rousseau DL, Bauman RP, Porto SPS. Normal mode determination in crystals. *J Raman Spectrosc.* 1981;10:253–290. doi:[10.1002/jrs.1250100152](https://doi.org/10.1002/jrs.1250100152)
41. Königstein JA, Mortensen OS. Laser-excited phonon Raman spectrum of garnets. *J Mol Spectrosc.* 1968;27:343–350. doi:[10.1016/0022-2852\(68\)90043-X](https://doi.org/10.1016/0022-2852(68)90043-X)
42. Mingsheng P, Mao HK, Dien L, Chao ECT. Raman spectroscopy of garnet-group minerals. *Chin J Geochem.* 1994;13:176–183. doi:[10.1007/BF02838517](https://doi.org/10.1007/BF02838517)
43. Nakamoto K. Infrared and Raman Spectra of Inorganic and Coordination Compounds. Part A: Theory and Applications in Inorganic Chemistry. 6th ed. Hoboken, NJ: John Wiley & Sons, Inc.; 2009. 419 p.
44. Kolesov BA, Geiger CA. Raman spectra of silicate garnets. *Phys Chem Minerals.* 1998;25:142–151. doi:[10.1007/s002690050097](https://doi.org/10.1007/s002690050097)
45. Moore RK, White WB, Long TV. Vibrational spectra of the common silicates: I. The garnets. *Am. Mineral.* 1971;56:54–71.